

Catalytic Role of the Substrate Defines Specificity of Therapeutic L-Asparaginase

Andriy Anishkin¹, Juan M. Vanegas², David M. Rogers², Philip L. Lorenzi³, Wai Kin Chan³, Preeti Purwaha³, John N. Weinstein³, Sergei Sukharev¹ and Susan B. Rempe²

¹ - Department of Biology, University of Maryland, College Park, MD 20742, USA

² - Center for Biological and Engineering Sciences, Sandia National Laboratories, Albuquerque, NM 87185-1315, USA

³ - Department of Bioinformatics and Computational Biology and Department of Systems Biology, University of Texas MD Anderson Cancer Center, Houston, TX 77230-1402, USA

Correspondence to Sergei Sukharev and Susan B. Rempe: sukharev@umd.edu; slrempe@sandia.gov

<http://dx.doi.org/10.1016/j.jmb.2015.06.017>

Edited by G. Hummer

Abstract

Type II bacterial L-asparaginases (L-ASP) have played an important therapeutic role in cancer treatment for over four decades, yet their exact reaction mechanism remains elusive. L-ASP from *Escherichia coli* deamidates asparagine (Asn) and glutamine, with an $\sim 10^4$ higher specificity (k_{cat}/K_m) for asparagine despite only one methylene difference in length. Through a sensitive kinetic approach, we quantify competition among the substrates and interpret its clinical role. To understand specificity, we use molecular simulations to characterize enzyme interactions with substrates and a product (aspartate). We present evidence that the aspartate product in the crystal structure of L-ASP exists in an unusual α -COOH protonation state. Consequently, the set of enzyme–product interactions found in the crystal structure, which guided prior mechanistic interpretations, differs from those observed in dynamic simulations of the enzyme with the substrates. Finally, we probe the initial nucleophilic attack with *ab initio* simulations. The unusual protonation state reappears, suggesting that crystal structures (wild type and a T89V mutant) represent intermediate steps rather than initial binding. Also, a proton transfers spontaneously to Asn, advancing a new hypothesis that the substrate's α -carboxyl serves as a proton acceptor and activates one of the catalytic threonines during L-ASP's nucleophilic attack on the amide carbon. That hypothesis explains for the first time why proximity of the substrate α -COO⁻ group to the carboxamide is absolutely required for catalysis. The substrate's catalytic role is likely the determining factor in enzyme specificity as it constrains the allowed distance between the backbone carboxyl and the amide carbon of any L-ASP substrate.

© 2015 Elsevier Ltd. All rights reserved.

Introduction

Bacterial type II L-asparaginases (L-ASP) have been used for over four decades to treat acute lymphoblastic leukemia [1] and other related forms of cancer [2,3]. Other applications of L-ASP include the food industry, where it is used to prevent the formation of acrylamides in foods with high starch content. L-ASP catalyzes the deamidation of both asparagine (Asn) and glutamine (Gln), which results in the formation of aspartate (Asp) and glutamate (Glu), respectively, and the by-product ammonia.

Although these two substrates differ in length by only one carbon, L-ASP demonstrates a significantly higher apparent affinity ($1/K_m$) and catalytic rate (k_{cat}) for Asn compared to Gln. As a result, enzyme specificity (k_{cat}/K_m) is $\sim 10^4$ times larger for Asn than for Gln (Fig. 1a) [4].

Reducing the availability of Asn in the blood is effective in killing certain types of cancer cells that are auxotrophic for Asn [5,6]. Side effects often linked to high glutaminase activity [7–11] pose a significant problem in L-ASP therapy and frequently preclude completion of the full treatment [12,13]. Yet,

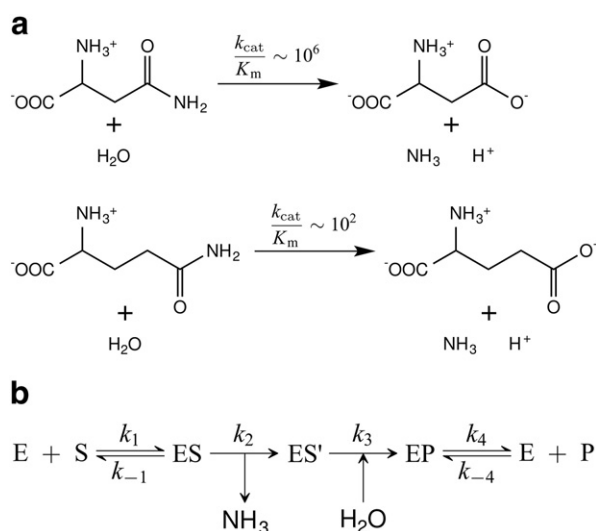


Fig. 1. (a) L-ASP catalyzes the conversion of Asn into Asp (top) and of Gln into Glu (bottom). L-ASP conversion of asparagine occurs with an $\sim 10^4$ higher specificity (k_{cat}/K_m) than for glutamine. (b) Model of the double-displacement mechanism supported by kinetic measurements. Upon formation of the enzyme–substrate complex (ES), ammonia (NH_3) is first cleaved before nucleophilic attack by water (H_2O) and final formation of the product (P). Forward and reverse rate constants are indicated by k_i and k_{-i} .

some glutaminase activity is considered necessary for a maximal anticancer effect on certain cell types [14]. This paradoxical behavior has been linked to the activity of another enzyme, asparaginase synthetase (ASNS), which converts glutamine into asparagine [15,16]. We recently showed that the necessity for glutaminase activity largely depends on the expression levels of ASNS [17]. Cancer cells that are ASNS negative are sensitive to both the wild-type L-ASP and a glutaminase-free mutant (Q59L). The wild-type enzyme is also effective against cells with low ASNS expression [17]. A better understanding of substrate specificity may provide a path toward optimizing asparaginase therapy [18–22] by engineering analogs with tailored ratios of asparaginase:glutaminase activity.

While the specific molecular details of L-ASP catalysis are not fully known, the wealth of functional and structural studies provides important insights on the reaction mechanism. L-ASP can deamidate other substrates besides asparagine and glutamine (including peptides with carboxy-terminal asparagine residues and Asn analogs such as succinamic acid), subject to the absolute requirement of a backbone carboxyl within two or three carbons from the carboxamide [23,24]. Early competition kinetics experiments strongly suggested a double-displacement (ping-pong) mechanism (Fig. 1b) proceeding through an aspartyl–enzyme intermediate [23,25]. That type of mechanism is further supported by functional muta-

genesis of the *Escherichia coli* [26,27] enzyme and structures of homologs from *Pseudomonas* [28] and *Erwinia chrysanthemi* [29,30].

Several residues in the *E. coli* enzyme catalytic site (Fig. 2) have been identified as important for asparaginase activity, including T12, Y25, T89, D90 and K162 [27,31–33]. The two well-conserved threonines, T12 and T89, have been proposed as possible nucleophiles in the formation of an enzyme–substrate intermediate, with individual mutations of these residues resulting in minimal change in K_m yet a

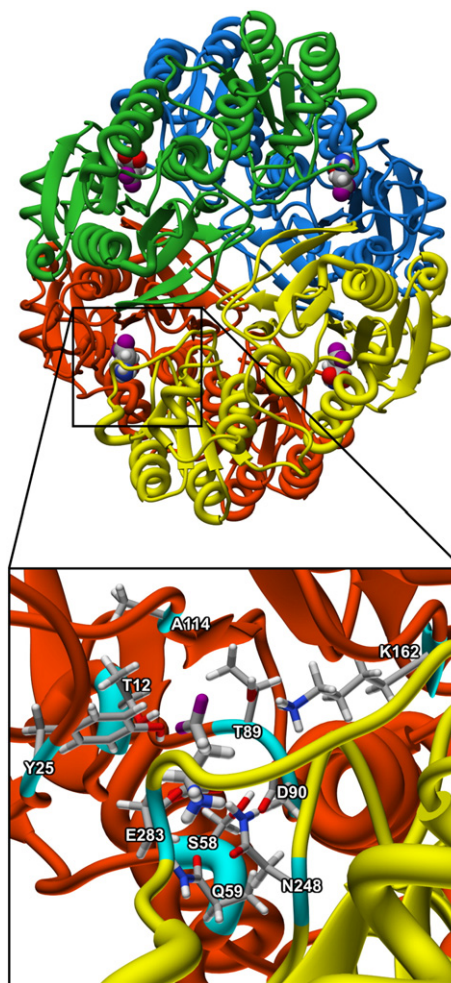


Fig. 2. Crystal structure of the *E. coli* L-ASP tetramer with bound aspartate product. The inset (bottom) highlights the positions of key residues (colored cyan) in one of four identical active sites. Those residues include T12, Y25, S58, Q59, T89, D90, A114 and K162 from one enzyme subunit (colored red), as well as N248 and E283 from the adjacent enzyme subunit (colored yellow). Thick tubes represent α -helical regions, and ribbons with arrows represent β -sheets. Atom color code: oxygens (red), nitrogens (dark blue), hydrogens (white) and carbons (gray). Side-chain oxygens of the Asp ligand are colored magenta for distinction.

drastic drop in the maximal reaction velocity [31,32]. Mutations of Y25 slow down the reaction turnover significantly [27]. Also, Y25's close spatial proximity to T12, observed in the crystal structure [34] (Fig. 2), led to the proposal that the tyrosine-glutamate Y25/E283 pair serves as a proton acceptor during nucleophilic attack [28]. Mutations of E283 have little effect on enzyme activity [29,33], however, and kinetic data suggest that Y25 instead plays a critical role in stabilizing the catalytic lid loop upon substrate binding [35]. Thus, questions about the specific nucleophile and proton acceptor remain open.

Our current atomic-level knowledge of the L-ASP reaction largely relies on the crystal structures [34,36] of the enzyme with bound Asp product. However, the different structural nature of Asn and Gln, compared with Asp, may result in changes in the orientation and corresponding contacts with the protein. Given the difficulty in obtaining a crystal structure of wild-type L-ASP with Asn or Gln, molecular simulations may be used to clarify many aspects of substrate binding and reaction mechanisms. A recent molecular simulation study [37] tested several possible deamidation mechanisms of Asn. With the use of electronic structure calculations, the work arrived at an energetically favorable process not requiring a covalent enzyme–aspartyl intermediate. However, the proposed reaction pathway disagrees with the experimentally supported, double-displacement mechanism (Fig. 1b) since water is involved in a direct nucleophilic attack of the substrate before cleavage of the ammonia group [37]. This discord may stem from the choice of initial configuration used in the electronic structure study.

The existing descriptions of the L-ASP catalytic mechanism have yet to explain how a one-carbon increase in substrate chain length that appears in Gln relative to Asn results in such a dramatic effect on the deamidation reaction (Fig. 1a). Furthermore, the unexplained absolute requirement of a backbone carboxyl within two or three carbon atoms from the carboxamide [23,24] may hint at a possible active role of the substrate during catalysis. Here, we address those two questions through a combined experimental and computational approach.

We first revisit the experimental kinetics of Asn and Gln degradation by L-ASP using a highly sensitive liquid chromatography–tandem mass spectrometry (LC-MS/MS) assay. We apply the assay to the clinically relevant *E. coli* enzyme (Elspar). Kinetic data collected in the presence of both substrates are interpreted in the context of substrate concentrations encountered in clinical settings. Kinetic data for pure substrates indicate that Asn and Gln induce different levels of mild cooperativity in the enzyme, suggesting that chemical features of the substrate can produce small changes to the global conformation of L-ASP. Since cooperativity is weak, no change is

expected to the reaction mechanism based on substrate occupancy. Hence, we conduct extensive classical molecular dynamics (MD) simulations to investigate the local structure of the L-ASP active sites and preferred positions of the product (Asp) and substrates (Asn and Gln). We find that each ligand establishes a different set of contacts with the enzyme that also modulates the intraprotein interactions of nearby residues. Finally, we use *ab initio* MD (AIMD) and electronic structure calculations to explore possible initial stages of the reaction that utilize the substrate's α -carboxyl as the primary proton acceptor. Our results give the first explanation as to why proximity of the α -COO⁻ group to the carboxamide is absolutely required for catalysis. A probabilistic assessment of conformations conducive for the initiation of catalysis also helps explain the higher k_{cat} and the lower K_{m} for Asn compared to Gln.

Results

Reexamining L-ASP kinetics and competition between substrates

We start exploration of selectivity, cooperativity and competition of the substrates by reexamining the kinetics of L-ASP deamidation. We recently developed a highly sensitive LC-MS/MS assay of L-asparaginase enzyme activity capable of simultaneous measurement of the four amino acids (Asn, Gln, Asp and Glu), as described in [Materials and Methods](#). The sensitivity of the assay is important to capture the behavior of the enzyme at all levels of substrate concentration since the apparent binding affinity for Asn is low ($K_{\text{m}} \sim 15 \mu\text{M}$ [4]). Given the large differences in the previously observed k_{cat} and K_{m} for Asn and Gln, a more accurate determination of these kinetic constants will be helpful in characterizing the competition and the dynamics of asparagine elimination in the presence of glutamine, as it occurs under physiological conditions in the blood plasma.

The deamidation kinetics of Asn show a clear pattern of cooperativity between subunits (Fig. 3a) and were consequently fitted to the Hill equation for reaction velocity v_0 ,

$$v_0 = \frac{V_{\text{max}}[S]^n}{K_{0.5}^n + [S]^n}, \quad (1)$$

where the half-occupation constant ($K_{0.5}$, analogous to the Michaelis constant, K_{m}) is defined by the substrate (S) concentration at which the reaction attains one-half its maximal velocity (V_{max}), and the Hill coefficient (n) describes the cooperativity between enzyme subunits for a given substrate. The apparent value of n for Asn is 1.5 ± 0.1 , while that for Gln is 1.1 ± 0.1 . Although cooperativity has not been

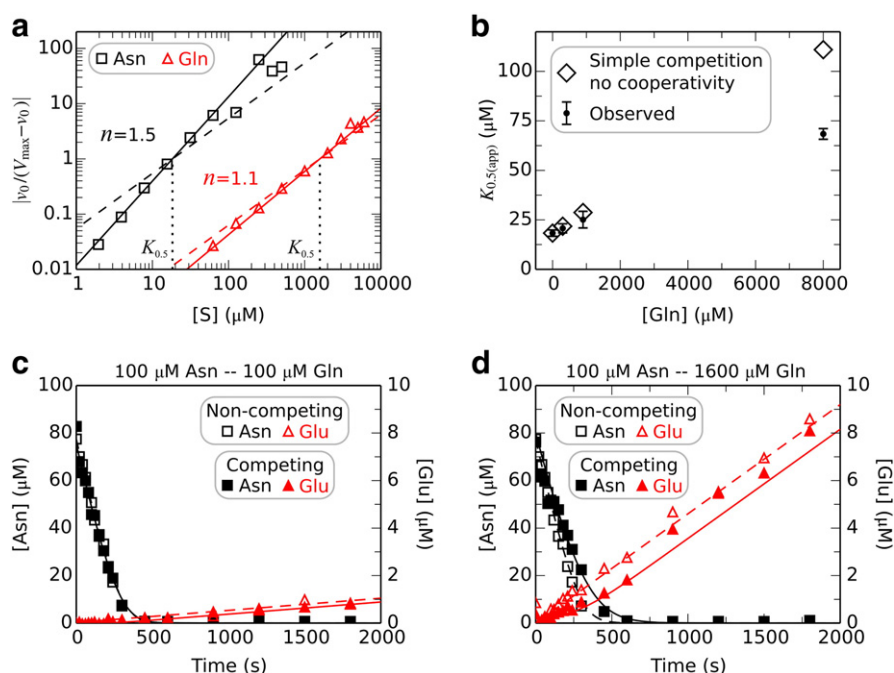


Fig. 3. Kinetics of substrate deamidation by L-ASP assayed by the LC-MS/MS technique. (a) Hill plots, $|v_0/(V_{\max} - v_0)|$ versus substrate concentration on a double-logarithmic scale, show the cooperativity of the enzyme in the degradation of Asn (squares) and Gln (triangles). Broken lines show the corresponding curves with no cooperativity ($n = 1$). Vertical dotted lines show the substrate concentration ($K_{0.5}$) needed to reach half the V_{\max} . (b) Apparent half-occupation, $K_{0.5(\text{app})}$, constants obtained for Asn degradation in the presence of competitive inhibitor Gln. Diamonds show the expected $K_{0.5(\text{app})}$ values assuming a simple competition scheme without cooperation [Eq. (2)]. (c) and (d) show time courses of Asn and Gln deamidation by 7.5 nM L-ASP for mixtures containing 100 μM Asn + 100 μM Gln and 100 μM Asn + 1600 μM Gln. Squares mark Asn depletion; triangles indicate Glu appearance; curves indicate theoretical predictions. Open symbols and broken lines show data and predictions for deamidation of each substrate separately (no competition) at the corresponding concentrations in each case. Filled symbols and continuous lines show data and predictions for deamidation of a mixture of the two substrates at the corresponding concentrations in each case. Inhibition of asparaginase activity increases with inhibitor (Gln) concentration.

reported previously for L-ASP, it has been observed in the type I bacterial asparaginase, with a Hill coefficient of 2.6 [38]. The observed turnover rate for Asn of $60 \pm 7 \text{ s}^{-1}$ is higher compared to previous values of $24\text{--}45 \text{ s}^{-1}$ [4,26,39], while the half-occupation constant ($K_{0.5}$) remains similar with a value of $18 \pm 2 \mu\text{M}$ compared to the previous K_m values of $\sim 15 \mu\text{M}$ [4]. The k_{cat} for Gln is higher than previous estimates, $2.2 \pm 0.3 \text{ s}^{-1}$ compared to $0.33\text{--}1.5 \text{ s}^{-1}$ [4,26,39], yet $K_{0.5}$ is considerably lower, $1600 \pm 400 \mu\text{M}$ compared to the K_m values of $3500\text{--}5200 \mu\text{M}$ [4,26,39]. A higher temperature ($T = 37 \text{ }^\circ\text{C}$) used here to mimic physiological conditions may account for increased k_{cat} relative to prior measurements carried out at room temperature ($T = 25 \text{ }^\circ\text{C}$). The observed k_{cat} is ~ 30 times greater, and apparent binding affinity ($1/K_{0.5}$) is ~ 80 times greater, for Asn than for Gln. The specificity constants ($k_{\text{cat}}/K_{0.5}$) of $3.3 \times 10^6 \text{ M}^{-1} \text{ s}^{-1}$ for Asn and $1.4 \times 10^3 \text{ M}^{-1} \text{ s}^{-1}$ for Gln indicate that *E. coli* L-ASP (Elspar) favors degradation of Asn over Gln

by a factor of 2400, approximately 10 times lower than previously reported [4].

While Asn is clearly the stronger competitor, reliable anticancer effects require deep Asn depletion down to submicromolar concentrations [14,40,41], where the more abundant Gln can outcompete the preferred substrate. Thus, we explore the competition between the two substrates for the active site in L-ASP by measuring the steady-state behavior for Asn degradation in the presence of varying concentrations of Gln. Steady-state kinetic parameters, including the half-occupation constant ($K_{0.5}$), the Hill coefficient (n) and the turnover rate (k_{cat}), are presented in Table 1 for all measured substrate conditions.

Given that the substrates affect the cooperativity of L-ASP differently, many kinetic constants may be needed to describe accurately the steady-state behavior during competition. Nevertheless, we expect that a simple competition scheme (no cooperativity) may predict the behavior of the

Table 1. Kinetic parameters for deamidation of individual and mixed substrates by L-asparaginase II

Experiment	$K_{0.5}$ (μM)	n	k_{cat} (s^{-1})	$k_{\text{cat}}/K_{0.5}$ ($\text{M}^{-1} \text{s}^{-1}$)
Pure Asn	18 ± 2 (~ 15) ^a	1.5 ± 0.2	60 ± 7 (24–45) ^a	3.3×10^6
Pure Gln	1600 ± 400 (3500–5200) ^a	1.1 ± 0.1	2.2 ± 0.3 (0.33–1.5) ^a	1.4×10^3
Asn + 300 μM Gln	21 ± 2	1.4 ± 0.1	72 ± 5	3.4×10^6
Asn + 900 μM Gln	25 ± 4	1.4 ± 0.2	67 ± 3	2.7×10^6
Asn + 8000 μM Gln	68 ± 3	1.0 ± 0.2	48 ± 9	0.71×10^6

^a Previously obtained values of $K_{0.5}$ (K_m) and k_{cat} (Refs. [4,26] and [39]) obtained at room temperature assuming no cooperativity between subunits.

apparent half-occupation constant, $K_{0.5(\text{app})}$, for Asn at inhibitor (Gln) concentrations near or below K_i ($K_{0.5}$ for Gln) with sufficient accuracy. If that is the case, the substrate concentration needed to reach half the maximum velocity will increase linearly with inhibitor concentration [I] according to

$$K_{0.5(\text{app})} = K_{0.5} + [I] \times K_{0.5}/K_i. \quad (2)$$

The values of $K_{0.5(\text{app})}$ (Fig. 3b) show good agreement with the simple competition scheme [Eq. (2)] for Gln concentrations below K_i (300 and 900 μM Gln), and the corresponding Hill coefficients and turnover rates remain roughly constant for these two cases (Table 1). However, the predicted simple competition value is significantly higher than the observed one (Fig. 3b) at high Gln concentration (8000 μM , $\sim 5 K_i$), and k_{cat} also decreases (Table 1), indicating a more complex competition behavior. In the case when the inhibitor suppresses the cooperativity of the substrate, the apparent Hill coefficient for enzyme competition is expected to approach 1.0 as the inhibitor reaches an infinite concentration [42], which is in good agreement with the value of $n = 1.0 \pm 0.1$ obtained for the highest Gln concentration (Table 1).

To further quantify the substrate competition, we measured the time courses of Asn depletion and Glu formation reactions in 1:1 and 1:16 (Asn:Gln) mixtures as compared with identical reactions performed with pure substrates (Fig. 3c and d). L-ASP (Elspar) at 7.5 nM concentration completely degrades pure 100 μM Asn ($\sim 5 K_{0.5}$) in a linear fashion within ~ 300 s. Gln, when present in equal concentration, has little influence on the time course of asparaginase reaction. In contrast, 1600 μM Gln ($\sim 1 K_i$) slows the reaction appreciably. Note that Glu appears with a measurable rate only after most Asn is degraded in the 1:1 mixture. The Gln-to-Asn ratio at which both product reaction rates equal each other is approximately 3000 for both competition experiments (Fig. 3c and d), which is in good agreement with the measured ratio of the Asn/Gln specificities ($k_{\text{cat}}/K_{0.5}$) of 2400.

Considering the kinetic parameters in the context of clinical application provides insights about the utility of substrate competition. At the physiological

blood plasma concentration of 800 μM Gln ($0.5 K_{0.5}$) and 50 μM Asn ($2.4 K_{0.5}$) [43], about 10% of the newly injected clinical variant of *E. coli* L-asparaginase will be occupied by Gln (according to v_0/V_{max}). The remaining enzyme will begin degrading Asn due to the higher probability of Asn entering the reaction (90% occupancy) and 30 times higher turnover rate (k_{cat}) relative to Gln. The enzyme will “switch” to Gln deamidation when Asn levels drop below 0.4 μM ($0.02 K_{0.5}$). Partial depletion of Gln consequently permits further decrease of Asn levels. Thus, the enzyme sequesters Gln precisely when Asn approaches the submicromolar concentration levels required for reliable anticancer activity. Our competition data well explain correlated changes of Asn and Gln levels recorded in clinical trials [11].

The finding that Asn and Gln induce different levels of mild cooperativity in L-ASP suggests that substrate binding can affect the global conformation of the protein to a limited extent, and these changes depend on the chemical features of the ligand. Nevertheless, weak cooperativity suggests that the reaction mechanism is unchanged by occupancy of multiple binding sites. Therefore, we focus on the local features of the active site to gain mechanistic insights. In particular, we characterize the local enzyme–ligand interactions for Asn, Gln and the enzymatic product Asp.

Protonation state of Asp product

Based on the crystal structure of *E. coli* L-ASP (PDB ID: 1NNS) [36] with the Asp product bound (Fig. 2), we use classical MD simulations to characterize how subtle chemical features, represented by different protonation states, modulate the enzyme–ligand interactions for the Asp ligand. This first step defines a control case that considers the structure and dynamics of the enzyme when occupied by the same ligand present in the crystal structure.

Under neutral conditions (pH of ~ 7) in bulk water, a conventional expectation is that the Asp ligand would be fully charged, with two unprotonated carboxyl groups. Close examination of the hydrogen-bonding geometry between the Asp ligand and the enzyme in the 3ECA [34] and 1NNS [36] structures,

however, suggests that this ligand exists instead in an unusual protonation state. Following previously reported analyses [44,45], we observe that the C—O—O hydrogen bond between one of the α -carboxyl oxygens of the ligand and the S58 hydroxyl oxygen lies close to the plane formed by the α -carboxyl group (Fig. 4a). The angle for this C—O—O hydrogen bond is near 130° , which is a feature commonly observed when the carboxyl is protonated [44]. Additionally, estimation of the acid dissociation constant (pK_a) of the α -carboxyl of the ligand Asp with the widely used PROPKA software [46,47] suggests an unusually high value (close to neutral pH), which also supports a protonated state.

We test the hypothesis of a protonated α -carboxyl on Asp through MD simulations of the tetrameric enzyme based on the 1NNS structure. Similar results are anticipated for the lower-resolution 3ECA structure since the active sites appear identical with 1NNS. The product ligand (Asp) is

put into different protonation states: backbone carboxyl protonated (α -COOH), side-chain carboxyl (γ -COOH) protonated, doubly protonated (α -COOH and γ -COOH) and no carboxyl protonation (the conventional charged state at neutral pH). The systems are simulated for 1 ns with restrained backbone atoms on the enzyme, which maintains the overall structure of the protein to mimic the low-hydration and high-packing-density conditions of the crystal. The orientations of these differently protonated Asp ligands and selected nearby enzyme residues are tracked relative to the starting crystal structure configuration (Fig. 4 and Fig. S1). Root-mean-square deviation (RMSD) values for the ligand atoms, as well as for the side chains of residues in contact with the ligand (see Fig. 4), quantify the structural differences.

These simulations support the hypothesis that the α -carboxyl group of Asp is protonated since the two simulations with an α -COOH Asp ligand (Fig. 4b and

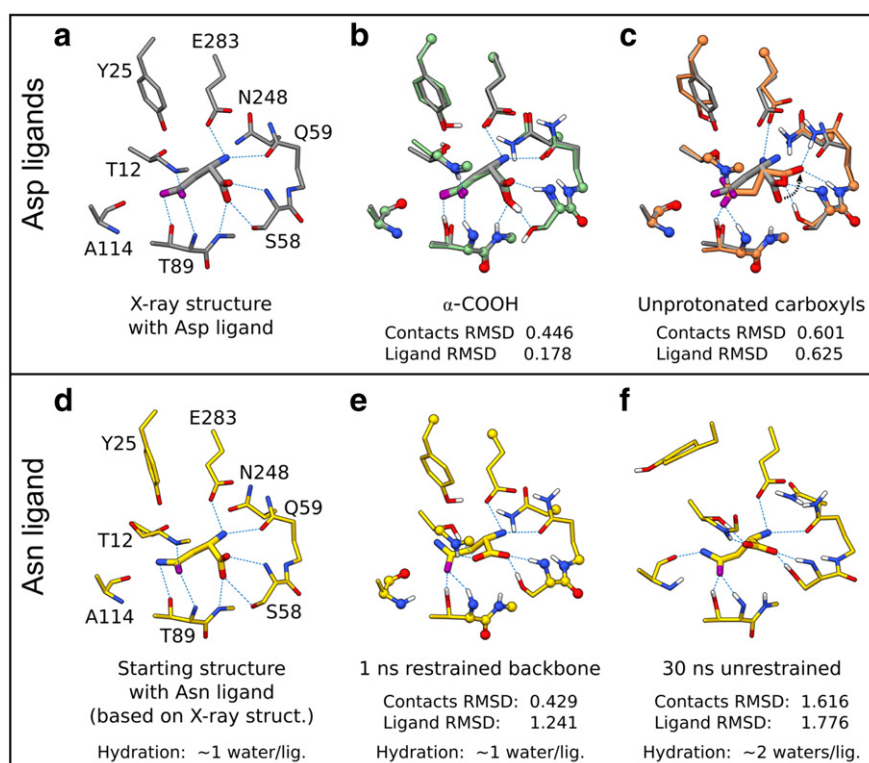


Fig. 4. Orientation of ligands in the active site. (Top panels) (a) The hydrogen-bonding pattern and geometry of the Asp ligand in the crystal structure suggest an unusual protonation state (see the text). (b) and (c) show the ligand position after 1-ns simulations under different protonation states while restraining the enzyme backbone atoms (shown as spheres). Broken black arrow in (c) illustrates the large reorientation of the ligand. Other possible protonation states of Asp are shown in Fig. S1. (Bottom panels) Asn ligand reorientation from the starting configuration (d) based on the position of the Asp ligand in the crystal structure. (e) Reorientation of the Asn ligand and nearby residues after 1-ns simulation while restraining the enzyme backbone atoms (shown as spheres). (f) Final position of the Asn ligand after simulating for 30 ns without restraints. Ligands are drawn with thicker bonds and only hydrogen atoms attached to the carboxyl groups shown for clarity. Broken lines highlight hydrogen bonds. Side-chain oxygens shown in magenta for distinction. “Contacts RMSD” values (\AA) relative to the crystal structure were calculated from protein residues in contact with the ligand: G11, T12, Y25, V27, G57, S58, Q59, G88, T89, D90, A114, M115, N248 and E283 (see [Materials and Methods](#)).

Fig. S1c) best reproduce the orientation of the ligand and nearby residues compared to the crystal structure (Fig. 4a).

While the α -COOH protonation state may seem unusual, the lower pH conditions (pH 5–6) and lower water content used during crystallization of the protein [34,36] would stabilize the α -COOH form of the Asp ligand (Fig. 4b). Crystallization conditions could also favor protonation of the side-chain carboxyl group. Protonation of only the γ -COOH group (Fig. S1b) seems unlikely, as seen by the large reorientation of the ligand and significantly larger RMSD value compared to the crystal structure. Asp protonated at both γ -COOH and α -COOH groups (Fig. S1c) appears less likely than the single α -COOH case (Fig. 4b) since the ligand RMSD value is slightly larger. Finally, the unprotonated Asp ligand (Fig. 4c) undergoes a significant reorientation during this short simulation time, which strongly supports our hypothesis that the conventionally anticipated, fully charged state of the product does not correspond to that observed in the crystal structure. To further validate the results observed for the α -COOH (Fig. 4b) and the unprotonated Asp (Fig. 4c), we extended the restrained backbone simulations for these two systems up to 30 ns. The observed trends persisted in each case.

Orientation and hydrogen-bonding network of the natural ligands (Asn and Gln)

While factors other than crystallization conditions may have contributed to the unusual protonation state of the bound Asp product discussed in the last section (i.e., proton transfer during catalysis), the protonation states of the two substrates entering the catalytic site are unambiguous. Under physiological conditions (neutral pH), Asn and Gln should have unprotonated carboxyls upon initial binding to the enzyme. We focus on this initial contact and simulate L-ASP with both substrates under physiological protonation states (α -COO⁻ and α -NH₃⁺). The same crystal structure used in the previous section defines the starting configuration for the protein and ligand (Fig. 4d).

Similar to the unprotonated Asp case (Fig. 4c), Asn quickly reorients (<1 ns) within the catalytic site and forms new hydrogen bonds with the nearby side chains (Fig. 4e) even while the protein backbone is still restrained. After 30 ns of simulation without backbone restraints (Fig. 4f), the established protein–ligand contacts remain in place. In addition, an increase in hydration and rearrangement of several nearby residues occurs. For example, Y25 loses contact with T12 and E283 in three out of the four subunits. In fact, Y25 is no longer near the ligand in those subunits.

A close-up view within the catalytic site of one enzyme subunit reveals important differences in the hydrogen-bonding networks for Asn and Gln ligands (Fig. S2), which are illustrated in a two-dimensional schematic (Fig. 5a) of the protein–substrate (blue

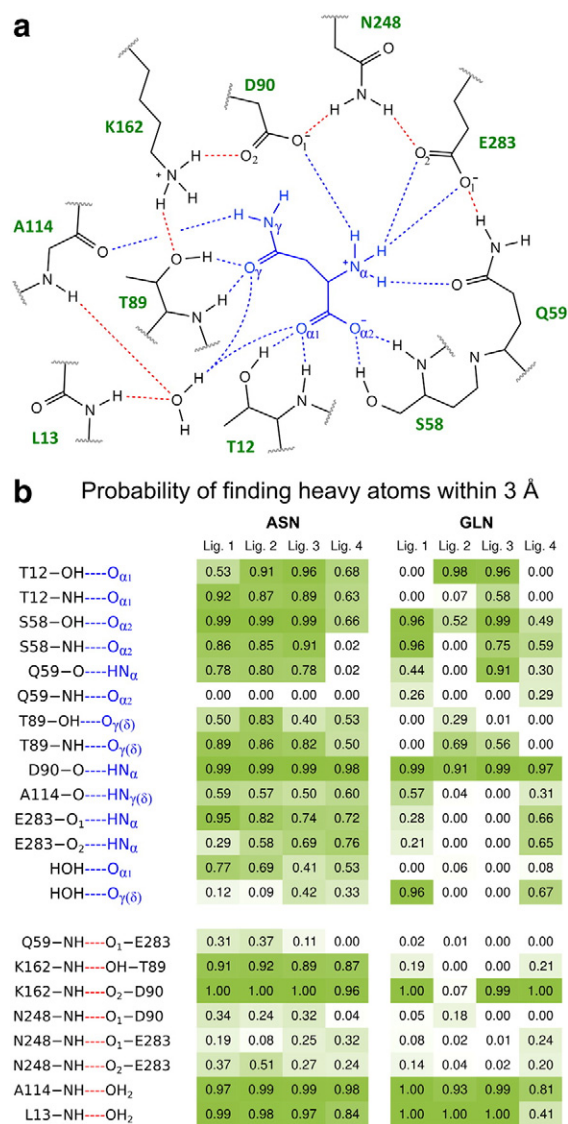


Fig. 5. (a) Contact map showing the hydrogen-bonding network in the L-ASP catalytic site for Asn ligand. Colored broken lines indicate protein–substrate (blue) and protein–protein (red) hydrogen bonds. (b) Probabilities of finding the heavy atoms of a given hydrogen-bonding pair within 3 Å during the last 20 ns of each simulation. Each box in the table is color coded (green = 1.0, white = 0.0) as a visual guide for interpretation.

broken lines) and protein–protein (red broken lines) contacts for the Asn ligand. For simplicity, we chose the labels O_{α1}, O_{α2} and N_α for the oxygens and nitrogen on the backbone end of the ligand, and O_γ and N_γ for the oxygen and nitrogen on the amide side chain. We quantified this hydrogen-bonding network for each subunit of the protein through the probability of finding the heavy atoms of a given contact within 3 Å during the last 20 ns of each simulation (Fig. 5b).

In the case of Asn, protein residues T12, S58 and T89 “clamp” onto the ligand and stabilize it through simultaneous interactions of the side-chain hydroxyls and backbone nitrogens with Asn’s amide and carboxyl oxygens. The positively charged α -amine of Asn is coordinated by Q59, D90 and E283, while the amide nitrogen forms hydrogen bonds with the backbone oxygen of A114. Although K162 and N248 do not contact the ligand directly, those residues may play an important role in maintaining the intraprotein hydrogen-bonding network. Additionally, a water molecule is trapped in a small cavity in the catalytic site, which is stabilized by hydrogen bonds with L13 and A114. This unique water remains in place throughout the simulation (in all four catalytic sites for all ligands), isolated from the rest of the water in the vicinity. That water often contacts the carboxyl and amide oxygens of Asn.

The additional carbon in the Gln ligand, compared to Asn, affects how Gln interacts with the catalytic site. The contact probabilities (Fig. 5b) in the case of Asn are uniform across the subunits for most interactions, while many appear to have a bi-modal distribution for Gln. In terms of the protein–substrate contacts, Gln is consistently able to establish contacts only with S58 and D90 through the α -amine and carboxyl groups, respectively. Close interaction between the Gln carboxyl oxygen and T12-OH is only seen in two of the subunits, and interaction of the amide oxygen with T89-OH is only sparingly seen (probability $P = 0.29$) in one of the subunits. The one-carbon difference between substrates also affects the intraprotein hydrogen-bonding network. Particularly, the contact between K162 and T89 is consistently observed with a high frequency ($P > 0.85$) in all four subunits in the case of Asn, while it occurs much less frequently ($P < 0.25$) and in only two subunits for Gln. Although the role of the trapped water molecule is unclear, it is consistently present near the ligand and in close contact with the protein (through the backbone nitrogens of L13 and A114) in all four subunits for both substrates. The dynamics of this water molecule are highly restrained, to a degree comparable to the ligand’s backbone.

The difference in the pattern and number of enzyme contacts for the two substrates translates into different mobility of the ligands. We quantify the mobility as the root-mean-square fluctuation (RMSF) from the average position in the last 10 ns of simulation. Compared to Asn, Gln is 49% more mobile in the catalytic site. For Asn and especially for Gln, the side chain is considerably more dynamic than the backbone.

Residues in the catalytic site that are in direct contact with the ligand are 29% more dynamic when the ligand is Gln compared to Asn, with the largest change in mobility occurring in the catalytic loop. Overall, mobility of both ligand and protein correlates inversely with the preference for the ligand (Asn > Gln) and indicates

that the presence of the ligand in the catalytic site significantly affects the dynamics and local structure of the enzyme active site.

Prediction and testing of the reaction initiation pathway

During nucleophilic attack, the hydroxyl proton of one of the proposed catalytic threonines (T12 or T89) must be transferred to a nearby electronegative atom, either directly or through a proton bridge. Focusing on T12, we observe that the side-chain hydroxyl of this residue is in frequent close proximity to one of the α -carboxyls of the Asn ligand ($O^{\alpha 1}$; see Fig. 5b), which suggests that this oxygen could play the role of proton acceptor (Fig. 6a, PT1) upon attack of the amide carbon (C^Y in Asn and C^O in Gln). Alternatively, earlier works proposed that the enzyme’s E283 could act as a proton acceptor by means of a proton bridge through Y25 (Fig. 6a, PT2). We compare the probabilities of those two nucleophilic attacks/proton transfers by taking the distances between the atoms involved in each case (i.e., atom pairs connected by arrows in Fig. 6a) and calculating a normalized distance (see Fig. 6). A normalized distance value of 1 corresponds to the atoms being in contact, and higher values correspond to the atoms moving apart.

Time traces of the normalized distances comparing the two possible proton transfers in the case of Asn suggest that the substrate’s α -carboxyl is close enough to act as a proton acceptor during nucleophilic attack by T12 (Fig. 6b). A similar trend is observed in the case of Gln (Fig. 6c) although there is more variability between subunits of the enzyme. Our results indicate that the alternative (PT2) proton transfer from T12 to E283 through Y25 is unlikely for either substrate since the atoms involved in the transfer are never found in close proximity at the same time during the course of the simulation. The likelihood of observing either proton transfer path is better illustrated in probability density plots (Fig. 6d), where we combine the normalized distances sampled independently over all four subunits in each case.

To test possible initiation mechanisms for nucleophilic attack by the enzyme’s T12 onto the amide carbon (C^Y) of the Asn substrate, we use AIMD simulations and electronic structure [quantum mechanics (QM)] methods. We assess the stability of reaction intermediates with AIMD and predict reaction energies ($\Delta E = E_{\text{products}} - E_{\text{reactants}}$) with QM. For each reaction tested, we steer the AIMD simulations by bringing two selected atoms within bonding distance in a stepwise manner, followed by release of the steering constraints, to observe the lifetime of the intermediate products (see [Materials and Methods](#)). Structures of reactant and product complexes for each reaction are also energetically

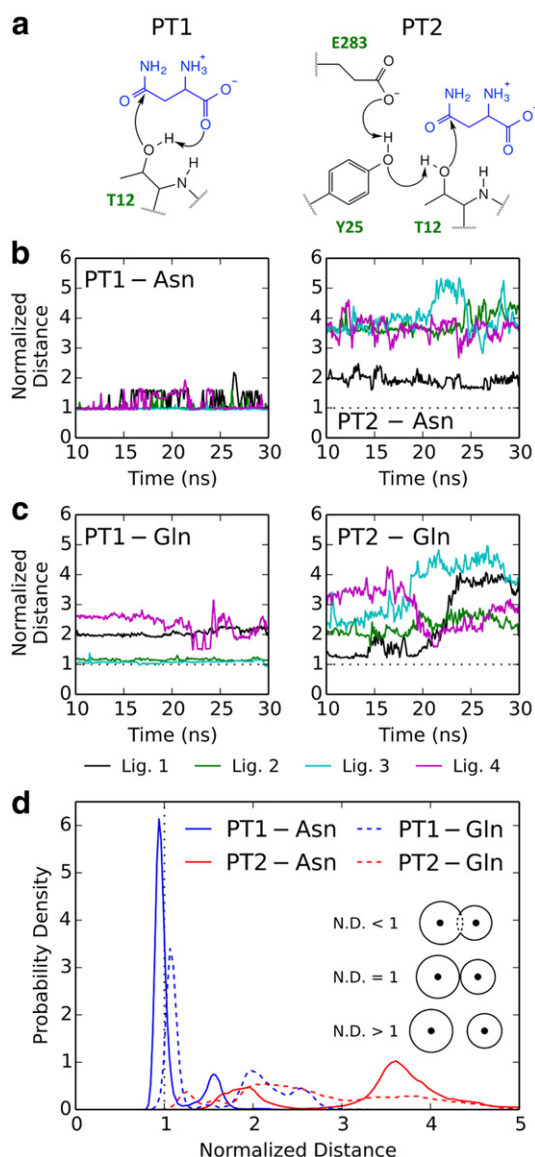


Fig. 6. Predicting atomic proximities for a nucleophilic attack of the substrate. (a) Two paths for nucleophilic attack by T12 hydroxyl O to Asn C γ (C δ in Gln) and the corresponding proton transfer: (1) to the α -carboxyl of the ligand (PT1) and (2) to E283 through Y25 (PT2). Normalized distances for each catalytic site occupied by (b) Asn, or (c) Gln. The normalized distance is obtained from the distance between each atom pair connected by arrows in each proton transfer pathway during the period from 10 to 30 ns, divided by the sum of the corresponding van der Waals radii (CHARMM27 parameters) and averaged over all pairs in each case. On (b) and (c), each time-dependent distance trace has been smoothed with a running average (100 ps window) for clarity. (d) Probability densities of normalized distances (all four catalytic sites combined) for the two pathways.

optimized and single-point energies are calculated with two different density functionals and large basis sets for comparison (see [Materials and Methods](#)).

The AIMD/QM system is composed of a subset of 18 of the enzyme's residues in the active site, including T12, Y25, S58, T89, K162, E283, the Asn substrate and the confined water molecule (see [Fig. 7a](#) and [Materials and Methods](#)). The coordinates for this subsystem were taken from a snapshot of the classical simulation at the end of the 1-ns period when the protein backbone atoms were restrained. We selected this snapshot due to the compactness of the active site ([Fig. S3](#)), which significantly reduces the computational cost yet retains the important structural features of the unrestrained system (see [Materials and Methods](#)). In the AIMD simulations, we also include four additional water molecules found near the substrate to provide a more realistic solvation environment for the Asn substrate. These waters are omitted in the structural optimizations and single-point energy calculations due to their unstructured nature, which prohibit consistent optimization results. Instead, solvation effects in the electronic structure calculations are included implicitly through a polarizable continuum model (see [Materials and Methods](#)).

Upon direct attack of asparagine C γ by the hydroxyl O of T12 and formation of the enzyme–substrate intermediate (E–Asn; [Fig. 7b](#) and [Fig. S4](#)), the hydroxyl proton spontaneously transfers onto the nearby carboxyl oxygen of the substrate (COO–H distance of 0.94 Å; [Fig. S4](#)). Spontaneous proton transfer occurs once the T12–O–C γ distance is less than 1.6 Å, indicating an energetic barrier at larger separations. The substrate's amide oxyanion that forms in the reaction product is stabilized by the hydroxyl proton of T89 (T89–OH–O distance of 1.55 Å; [Fig. S4](#)) and a proton of the trapped water molecule (HOH–O distance of 1.72 Å; [Fig. S4](#)). However, once the system is allowed to evolve naturally over time, we observe that the enzyme–substrate intermediate is unstable ([Fig. S4c–f](#)) and quickly (<0.025 ps) relaxes back to the starting configuration. The kinetic instability of the E–Asn intermediate suggests a small difference between the energy of the products and the transition state. While obtaining a transition state structure for this reaction and its corresponding energy is beyond the scope of this study, the energy difference (ΔE) for the optimized structures in this case is ~ 30 kcal/mol ([Table 2](#)).

Protonation of the substrate's amide oxygen prior to nucleophilic attack may stabilize the enzyme–substrate intermediate by preventing formation of an electron-unpaired oxyanion. That proton could originate from the enzyme's nearby lysine (K162) and transfer to the ligand through T89 (first step in [Fig. 7c](#)). The amine of K162 has a high probability of being hydrogen bonded to the hydroxyl O of T89 and so does the T89–OH to the ligand's amide oxygen (see [Fig. 5b](#)). Additionally, experimental work has suggested that K162 acts as a proton buffer for T89 since it may

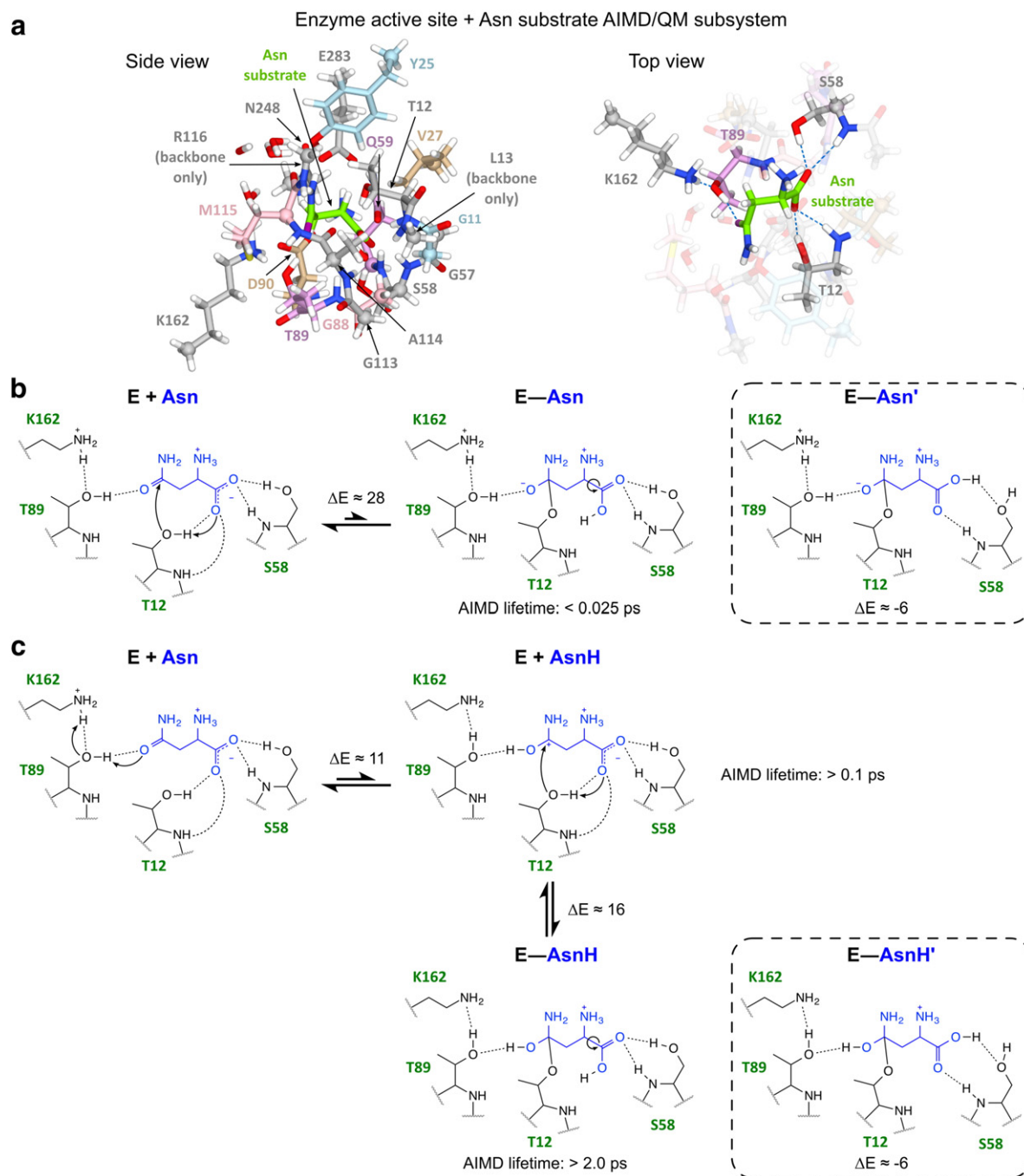


Fig. 7. Testing the kinetic stability and energetics of possible initiation mechanisms for nucleophilic attack on the substrate by the enzyme residue T12. (a) Enzyme + Asn substrate AIMD/QM subsystem (see [Materials and Methods](#)). Asn carbon atoms are shown in green, and side-chain oxygen is in magenta, for distinction. A chemical reaction is driven in each case until two selected atoms are bonded (see [Materials and Methods](#)). (b) Direct nucleophilic attack of the substrate's γ carbon by the hydroxyl O of T12 (see also [Fig. S4](#)). (c) Two-step nucleophilic attack by T12 through preprotonation of the substrate amide oxygen by the K162-T89 proton bridge (see [Figs. S5–S7](#)). All ΔE given in kilocalories per mole (kcal/mol) for the M062X functional (see [Table 2](#)). The E-Asn' and E-AsnH' configurations on the right (enclosed by broken boxes) are lower-energy configurations resulting from α -COOH—S58 reorientation and consequent “paired” instead of “clamped” hydrogen bonding.

have an unusually low pK_a [32]. Such a protonated intermediate ([Figs. S5 and S6](#)) appears to be metastable (>0.1 ps), depending on the initial condi-

tions. As an example, keeping the protonated amide oxygen of the ligand oriented toward the hydroxyl O of T89 (the proton source) makes the intermediate stable

Table 2. Energy differences for energy-optimized reactants and products in nucleophilic attack

	Reactants	Products	ΔE^a M062X ^b (kcal/mol)	ΔE^a ω B97X-D ^b (kcal/mol)
Direct nucleophilic attack by T12	E + Asn	E–Asn	28	32
With α -COOH—S58 reorientation	E–Asn	E–Asn'	–6	–6
Two-step nucleophilic attack by T12	E + Asn	E + AsnH	11	12
	E + AsnH	E–AsnH	16	22
		Total	27	34
With α -COOH—S58 reorientation	E–AsnH	E–AsnH'	–6	–7

^a $\Delta E = E_{\text{products}} - E_{\text{reactants}}$.

^b Single-point energies calculated with the 6-311++G(2d,2p) basis set.

for ~ 0.1 ps (Fig. S5) before returning to the starting configuration. That time is short, but considerably longer ($\sim 4\times$) than the intermediate formed by direct attack of the ligand by T12. In contrast, allowing the proton to point away from T89 significantly improves the stability of the protonated intermediate beyond 0.75 ps (the length of the simulation; Fig. S6). The energy difference for this E + Asn \rightarrow E + AsnH intermediate reaction step is ~ 12 kcal/mol (Table 2), which is less than half the overall reaction energy for direct nucleophilic attack described above.

Similarly to the direct T12 attack (Fig. 7b), nucleophilic attack by T12 onto the amide-protonated substrate (second step in Fig. 7c) results in spontaneous transfer of the T12 hydroxyl proton onto the nearby carboxyl oxygen of the substrate (COO–H distance of 1.06 Å; Fig. S7). In this case, however, the enzyme–substrate intermediate is stable for the duration of the 2.0-ps AIMD simulation (Fig. S7c–f). Protonation of the substrate's amide oxygen appears to improve the kinetic stability of the E–AsnH tetrahedral intermediate significantly ($\sim 100\times$) compared to the E–Asn case. Moreover, the energy difference for this second E + AsnH \rightarrow E–AsnH intermediate step is ~ 16 kcal/mol (Table 2), similar to the first protonation step. Adding the second nucleophilic attack with the first amide protonation step places the overall energy difference for the E + Asn \rightarrow E + AsnH \rightarrow E–AsnH nucleophilic attack ~ 30 kcal/mol (Table 2).

Although the overall energy difference between product and reactant complexes in both nucleophilic attacks tested is similar, the second nucleophilic attack via the intermediate amide protonation step is a more likely pathway for the reaction due to the increased kinetic stability, as well as the division into two lower-energy steps. We note that the relatively large values of the energies reported in Table 2 may be due to constraining the α carbons in the electronic structure calculations. Freezing the positions of the α carbons maintains the relative orientation of the enzyme residues similarly to the native structure yet limits the extent of the structural/energetic optimizations. Therefore, the constraints likely result in overestimation of the calculated single-point energies.

While the backbone amide and hydroxyl groups of S58 form a “clamping” hydrogen-bonding pattern with the α -COO[–] of the Asn ligand prior to nucleophilic attack, with both protons of S58 on the same carbonyl oxygen (Fig. 5 and Fig. S2), the substrate's protonated α -COOH in the covalently bound intermediates (E–Asn and E–AsnH) may prefer to hydrogen-bond differently. The 2-ps AIMD trajectory of the second nucleophilic attack by T12 (Fig. S7) shows that the hydroxyl group of S58 loosens from the carbonyl oxygen in the substrate's α -COOH and begins to transition into a “paired” hydrogen-bonding pattern (Fig. S7f). Optimization of the E–Asn and E–AsnH structures, which promotes reorientation of the substrate α -COOH and S58 hydroxyl groups (E–Asn' and E–AsnH'; Fig. 7b and c), shows that the paired hydrogen bonding is energetically favored over the clamping pattern (by ~ 6 kcal/mol; see Table 2).

Returning to the results from the classical MD simulations, we compute the normalized distance for this latter mechanism (Fig. 7c) of nucleophilic attack by T12 in which substrate protonation occurs at the amide oxygen in addition to the α -COO[–] (Fig. S8a). A comparison of the two ligands (Fig. S8b and c) suggests that a double-protonation event would be much more likely to occur for Asn than for Gln. We note that the prerequisite to have all four atom pairs in close proximity at the same time prior to catalysis largely depends on the lifetime of the first intermediate (substrate protonated on the amide oxygen) and whether there is sufficient time for the nucleophilic attack to take place while that intermediate still exists.

Discussion

Using a sensitive LC-MS/MS technique to characterize enzyme kinetics, we demonstrated that the two natural substrates are degraded by L-ASP simultaneously and in a regime close to simple competition. The substrates induce different levels of cooperativity between subunits, with Asn having a higher Hill coefficient ($n = 1.5$) compared to Gln ($n = 1.1$). Those results suggest that chemical features of the substrate can produce small changes to the global conformation

of L-ASP. While cooperativity increases the level of complexity needed to model steady-state kinetics, our data show that enzyme inhibition by Gln can be described well by a simple competitive inhibition scheme at physiological concentrations of the two substrates ($<K_{0.5}$ for Gln). We also obtained accurate kinetic constants for L-ASP at physiological temperature. Due to a specificity ($k_{cat}/K_{0.5}$) that is 10 times larger than previously found for Gln, the present results yield a ratio of Asn:Gln specificities of 2400 ($\sim 10^3$) compared to the previous value of $\sim 10^4$ determined under room-temperature conditions.

The refined Asn:Gln specificity ratio (2400) indicates that Gln will be degraded with efficiency that is about 1 order of magnitude higher than estimated previously [4,26,39]. The role of L-ASP glutaminase activity in cancer therapy and adverse side effects has been discussed previously [7–11]. Our kinetic data lead to the simple conclusion that, with the given kinetic parameters, competition for the catalytic site will be most pronounced when Asn concentration approaches the submicromolar level required for a reliable therapeutic effect. At that moment, glutaminase activity becomes necessary to deplete the nonpreferred, but highly abundant, Gln in order to decrease the level of Asn further. The predicted kinetic relationships capture the phenomenology of tight correlation between Asn and Gln concentrations reported in clinical trials [11]. The need to overcome kinetic block by Gln may help explain why optimal Asn depletion requires $\geq 90\%$ depletion of Gln to kill malignant cells in the blood [14].

Guided by the small values observed for enzyme cooperativity, which suggests that the catalytic mechanism is unaltered by substrate occupancy, we used molecular simulations to investigate the local structure of the L-ASP active sites. We showed that the specific chemical features of each ligand (Asp, Asn and Gln) affect both protein–ligand and protein–protein interactions.

Our initial analysis of the crystal structure of L-ASP with the product Asp and multiple MD simulations with different protonated forms of Asp indicated that the Asp ligand in the crystal structure is likely protonated at the α -carboxyl group. That unusual protonation state determines the set of protein–ligand interactions that formed the basis for prior interpretations of catalytic mechanism. Those interactions between enzyme and product differ from the ones observed in simulations of the enzyme with the substrates, which motivates a new mechanism.

Molecular simulations of L-ASP with Asn and Gln also revealed significant differences in interactions and mobility between the two substrates. Starting in the same protein and ligand configuration as in the crystal structure, Asn undergoes a considerable reorientation in the catalytic site of L-ASP early in the simulation (< 1 ns) and forms a new hydrogen-bonding

network with nearby residues. Although Gln is able to establish many of the same contacts with the enzyme, the additional carbon limits Gln to forming only a small subset of those contacts at any given time. The larger number of protein–ligand and intraprotein (near the catalytic site) hydrogen bonds, in the case of Asn, favors interaction with the enzyme and also lowers the mobility of the ligand in the active site, therefore accounting for the lower value of $K_{0.5}$ for Asn compared to Gln.

The classical MD simulations further suggested that the α -carboxyl in both substrates could act as a proton acceptor during nucleophilic attack. That conclusion resulted from observations of T12 (one of the candidates for nucleophilic attack) in close proximity and hydrogen bonding of the T12 side-chain hydroxyl to the α -carboxyl in both substrates.

Prior works have reported other instances when substrate molecules participated in catalytic reactions. For example, substrate backbone atoms have been shown to stabilize or directly participate in enzymatic reactions [48,49]. The α -carboxyl of glutathione has also been shown to act as a proton acceptor during catalysis by the glutathione transferase A1-1 [50]. Recall that prior experiments reported that a free carboxyl group on the backbone of L-ASP-catalyzed substrates in proximity to the amide group is required for catalysis [24]. An α -carboxyl group of the ligand that acted as the proton acceptor during nucleophilic attack would help explain that observation. Here, preliminary experimental results show that the substrate analogs homoglutamine and 3-aminobutanamide, in which the substrate α -carboxyl is too distant from the amide carbon or not present, are not degraded by L-ASP (see [Materials and Methods](#)). Those experimental results support our hypothesis.

Our *ab initio* simulations and electronic structure energy calculations provide further support for the substrate proton acceptor hypothesis by showing spontaneous proton transfer to the substrate (Asn) α -carboxyl and formation of a reasonably stable intermediate complex following a steered nucleophilic attack by T12. The resulting paired hydrogen-bonding pattern between S58 and the protonated α -carboxyl of the covalently bound enzyme–substrate intermediate (E–AsnH') resembles not only the geometry observed in the crystal structure with Asp ligand (Fig. 4a), but also the geometry of the crystal structure of the T89V mutant (Fig. 8). While crystallization conditions may stabilize unusual protonation states of the ligand, it is also plausible that the crystal structures (of the wild type and T89V mutant) provide a glimpse into the intermediate steps of nucleophilic attack. An alternate coordination of the ligand by S58 postnucleophilic attack, relative to prenucleophilic attack, may be a feature of the enzyme that specifically stabilizes the intermediate complex and prevents “backflow” of the proton to the

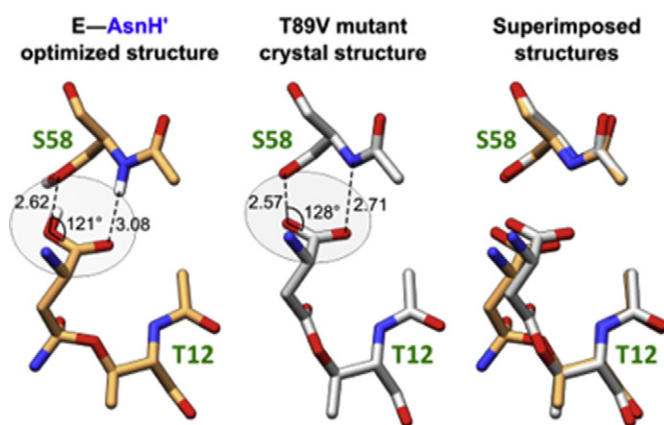


Fig. 8. Hydrogen-bonding pattern in two covalently bound enzyme–ligand intermediate structures: (left) optimized enzyme–substrate complex (E–AsnH⁺) from electronic structure calculations, (middle) enzyme–aspartyl (E–Asp) intermediate structure of the crystallized T89V mutant (PDB ID: 4ECA) and (right) structures superimposed. In both cases, S58 forms “paired” hydrogen bonds with the ligand’s α -carboxyl group, and the S58 hydroxyl oxygen lies in the same plane (gray disk). The orientation here resembles that of the product in the wild-type crystal (E + Asp; Fig. 4a), but differs from a “clamp” formed on the substrate prior to nucleophilic attack (E + Asn; Fig. 4f).

T12 hydroxyl donor, thus facilitating nucleophilic attack by T12.

Our results also bring into question the stability of the negatively charged (oxyanion) tetrahedral enzyme–ligand intermediate (observed lifetime of less than 0.025 ps). Guided by our contact data and previous experimental observations, we tested the possibility of stabilizing the tetrahedral intermediate by first protonating the amide oxygen of the Asn substrate by a proton transfer from K162 through T89, which in itself may be stable for longer than 0.1 ps. Protonation of the amide oxygen of Asn significantly increases the stability (>2.0 ps) of the enzyme–substrate intermediate after nucleophilic attack by T12. An initial nucleophilic attack that first requires protonation of the amide oxygen of the ligand through the K162–T89 proton bridge could help explain the increased catalytic rate observed for Asn compared with Gln. The present studies support a substrate amide preprotonation mechanism since K162 and T89 are frequently found in close proximity during occupation by the Asn substrate, but not Gln. That protein–protein interaction could improve the likelihood of a successful nucleophilic attack by T12 (Figs. S7 and S8) and therefore increase the observed k_{cat} for Asn *versus* Gln.

While the current study highlights the molecular determinants of substrate binding and the likely initial stages of reaction, the subsequent stages of the reaction and their corresponding energy changes remain to be explored by *ab initio* calculations. Furthermore, the dynamics of product release may largely depend on the final protonation state of ligand and enzyme. Studies for these two important aspects of L-ASP function are currently underway through classical MD and AIMD simulations.

In summary, our experimental and simulation results suggest that interactions with the protein are largely dependent on the specific structural features of the ligand. Furthermore, our data strongly support a new hypothesis that the substrate itself

plays a critical catalytic role in the L-ASP mechanism of deamidation by providing its own carboxyl as a base that abstracts the proton and thus activates a catalytic threonine. This catalytic role imposes a constraint on the allowed distance between the backbone carboxyl and the amide carbon of any L-ASP substrate, and it is likely the determining factor in the specificity of the enzyme.

Materials and Methods

Experimental kinetics

We recently developed a sensitive LC-MS/MS assay for direct assessment of L-asparaginase enzyme activity by simultaneous measurement of the four relevant amino acids: substrate Asn, product Asp, substrate Gln and product Glu [51]. The LC system was an Agilent 1290 infinity ultrahigh performance system coupled to an Agilent 6460 triple quadrupole mass spectrometer. The four amino acids were separated on a Zorbax SB-C18 column (3.0 mm \times 100 mm, 1.8 μm) using a mobile phase consisting of 0.3% heptafluorobutyric acid and 0.5% formic acid in (A) water and (B) acetonitrile. The LC gradient conditions were as follows: 0–2 min = 0% B; 2.01–2.5 min = 0–5.0% B; 2.51–3.5 min = 90.0% B; and 3.51–6 min = 0% B. The column temperature was 25 $^{\circ}\text{C}$; injection volume was 5 μL , and flow rate was 0.4 mL/min. The MS conditions included gas temperature at 300 $^{\circ}\text{C}$, drying gas flow at 7 L/min, nebulizer pressure at 50 psi, sheath gas temperature at 325 $^{\circ}\text{C}$, sheath gas flow at 10 L/min, capillary voltage at 3750 V, nozzle voltage at 0 V and dwell time at 20 ms. Multiple reaction monitoring transitions used for quantitation were 133.1 \rightarrow 74, 134.1 \rightarrow 74, 147.1 \rightarrow 84 and 148.1 \rightarrow 84 for Asn, Asp, Gln and Glu, respectively. Isotopically labeled internal standards included $^{13}\text{C}_4$ - $^{15}\text{N}_2$ -Asn, $^{13}\text{C}_4$ - $^{15}\text{N}_2$ -Asp, $^{13}\text{C}_5$ - $^{15}\text{N}_2$ -Gln and $^{13}\text{C}_5$ - $^{15}\text{N}_2$ -Glu, which were spiked into the methanol (MeOH) quenching solution at the optimized concentration of 10 μM . Limits of detection were 1.0, 0.5, 1.75 and 3.17 nM for Asn, Asp, Gln and Glu, respectively, with linearity ranging up to 1000 μM and r^2 of 0.998, 0.995, 0.991 and 0.996. The r^2 values are

coefficients of determination derived from linear regression of the standard curve from 0 to 1000 μM . Calibration curves were run using amino acids diluted in mobile phase A and 50% methanol.

The clinically used enzyme variant of *E. coli* type II L-asparaginase (Elspar®) was purchased from Ovation Pharmaceuticals. Enzyme reactions were performed at Elspar concentrations of 5 and 20 nM to assess Asn and Gln deamidation kinetics, respectively. Reactions included 2–1000 μM Asn or 63–8000 μM Gln and 23 mM Tris buffer (pH 8.5) and a temperature of 37 °C. Time courses of Asn or Gln deamidation by 7.5 nM Elspar with single substrates and mixtures of substrates were also measured. Mixtures spanned substrate Asn-to-Gln ratios from 1:1 to 1:16. At time points ranging from 0 to 30 min, reaction aliquots were quenched in 80% final MeOH containing the aforementioned four internal standards. Samples were then filtered through a protein precipitation plate and the filtrates were diluted further in mobile phase A, making the final dilution 20-fold. We determined that the rate of product formation (v_o) for the two substrates varies linearly over a wide range of substrate concentrations through 2 min (Asn) and 50 min (Gln).

In addition to asparagine and glutamine degradation, mixtures of 10 mM 2-amino-5-carbamoylpentanoic acid (homoglutamine) or 10 mM 3-aminobutanamide (3-AB) were also incubated with 1.8 μM Elspar in 23 mM Tris buffer (pH 8.0) at 37 °C for 24 h. No detectable product formed.

Steady-state kinetic parameters were determined from the initial velocity (v_o) versus substrate concentration curves using the Hill equation [see Eq. (1)] to account for cooperativity between enzyme subunits. The half-occupation constant $K_{0.5}$ is defined by the substrate concentration at which the reaction attains one-half its maximal velocity (V_{max}). The Hill coefficient, n , describes the cooperativity of the enzyme for a given ligand, with $n = 1$ indicating no cooperativity and $n > 1$ indicating positive cooperativity. The enzyme turnover rate, k_{cat} , was determined from the maximal velocity and the total enzyme concentration, $k_{\text{cat}} = V_{\text{max}}/[E]_o$. Asn and Gln deamidation kinetics were measured for the pure substrates, as well as for Asn in the presence of 300, 900 and 8000 μM Gln inhibitor. The resulting kinetic parameters are shown in Table 1. All velocity profile experiments were repeated at least three times, and the kinetic parameters were obtained by nonlinear fitting of the data to Eq. (1) using the SciPy tools [52].

In addition to the steady-state kinetics, time courses of Asn and Gln deamidation were also measured for each substrate separately and for two competing conditions (100 μM Asn + 100 μM Gln and 100 μM Asn + 1600 μM Gln), as shown in Fig. 3. Given the complexity of the kinetic equations needed to describe the different cooperativities of the substrates in different enzyme occupation states accurately, we modeled the approximate time behavior of the product release and substrate degradation using the conventional Michaelis–Menten equation with effective kinetic constants that provided the best fit for all curves shown in Fig. 3c and d. These effective constants ($k_{\text{cat}} = 72 \text{ s}^{-1}$ and $K_m = 19 \text{ }\mu\text{M}$ for Asn; $k_{\text{cat}} = 2 \text{ s}^{-1}$ and $K_m = 1900 \text{ }\mu\text{M}$ for Gln) were used to integrate the ordinary differential equations based on the initial substrate and enzyme concentrations using the SciPy tools [52].

Classical simulations

The tetrameric biological assembly of the crystal structure of *E. coli* L-asparaginase (PDB ID: 1NNS) [36] was used as a template for all molecular simulations. The catalytic site in this structure is occupied by the product aspartic acid. Simulations included all residues (1–326) resolved in the crystal structure. Molecular transformations, assembly of the simulation cell and computational analysis were performed with VMD [53] version 1.8 using custom-written Tcl scripts. All molecular visualizations and three-dimensional renderings were performed with the UCSF Chimera package version 1.10 [54]. For substrates other than aspartic acid (asparagine, glutamine), the VMD plugin PSFGEN was used to preserve the coordinates of the backbone and identical atoms of the substrate in the crystal structure and was used to derive the coordinates of any additional atoms. The N- and C-termini of the protein were modeled in the charged state. For the remaining amino acids, the dissociation state was estimated using the PROPKA[†] server [55,56]. All water molecules resolved in the crystal structure were retained during hydration of each system, and ~51,000 water molecules (TIP3P) were added to the cubic simulation cell (122 Å side). Sufficient sodium (137) and chloride (125) ions were added to neutralize the net charge of the protein (–12) and provide a salt concentration of 0.13 M.

Following energy minimization, we simulated each system for 1 ns with harmonic restraints on the backbone atoms (1 kcal/mol/Å² spring constant). Selected Asp systems were further simulated with restrained backbone atoms for up to 30 ns. After the initial 1-ns simulation with restrained backbone, assemblies with Asn and Gln were simulated up to 30 ns without restraints. All simulations were performed in the NPT ensemble using the NAMD2 simulation package [57] with the CHARMM27 force field parameters, including the grid-based CMAP correction [58,59]. The time step for all simulations was 1 fs, with coordinates saved every 1 ps. Pressure was maintained constant at 1 atm using the Langevin piston method, and the temperature was maintained at 310 K using the Langevin thermostat with a coupling coefficient of 1 ps⁻¹. Long-range electrostatics were calculated using the particle-mesh Ewald method with a real-space cutoff of 10 Å and a Fourier grid spacing of 1 Å. Nonbonded Lennard-Jones interactions were calculated using a switching function starting at 8.5 Å with a cutoff of 10 Å. Electrostatic forces were updated every 4 steps and Lennard-Jones interactions were updated every 2 steps. Simulations were conducted at the High Performance Computer Cluster at the University of Maryland, College Park, and at the RedSky Supercomputer at Sandia National Laboratories.

Ab initio simulations

Atomic coordinates for *ab initio* simulations of Asn in the active site of L-ASP were taken from a snapshot of the classical MD simulation near the end of the first 1 ns with restrained backbone atoms. In this selected configuration, the ligand orientation and protein contacts are stable (see Fig. 4) yet the active site is compact, which significantly reduces the computational costs. The 239-atom system (see Fig. S3) included four water molecules and residues

G11, T12, L13 (backbone atoms only), Y25, V27, G57, S58, Q59, G88, T89, D90, G113, A114, M115, R116 (backbone atoms only), K162, N248 and E283.

Comparison of the selected conformation to the initial crystal-like arrangement, and the structure after the 30-ns unrestrained simulation, shows that the contacts of the ligand with the enzyme are well maintained through the unrestrained stage (Fig. 4e and f), with slightly decreased frequencies. The slightly reduced enzyme–ligand contacts are due to the thermal fluctuations of the system at full hydration, which are unimpeded by the molecule packing in the crystal. Importantly, there is a crucial change present in the structure used for AIMD simulations (Fig. 4e), compared to the crystal-like arrangement (Fig. 4d), that persists through the whole unrestrained stage: strengthening of the contact between T12 and the backbone carboxyl of the ligand in contrast to the terminal carboxyl indicative of Asp in the crystal structure. That change makes the configuration at the end of the restrained simulation period already consistent with our proposed mechanism of the backbone carboxyl of the ligand as the primary acceptor of the proton from the T12 hydroxyl.

Amino acids not connected to other residues, or at the end of a chain, were terminated at the C^α position (as a methyl group) to avoid spurious effects from charged termini such as COO[−] and NH₃⁺. The α carbons of all protein residues were fixed to maintain the structural integrity of the active site during the simulations, except in the case of residues T12 and T89 because they were involved in nucleophilic attack or proton transfer.

Ab initio simulations were performed using the Vienna *ab initio* simulation package VASP software [60–62]. Atomic interactions were calculated with the generalized gradient approximation exchange–correlation density functional of Perdew, Burke and Ernzerhof (PBE) [63,64] and project-d-augmented wave pseudopotentials [65] incorporating only valence electrons. PBE is a pure functional of broad applicability, with good performance on biologically relevant systems [66,67] that is comparable to hybrid functionals such as the commonly used B3LYP [68–70]. The pure functional form of PBE also offers a significant speed-up compared to hybrid functionals in VASP due to lower computational cost at each iteration (no Hartree–Fock exchange calculated) and faster convergence of the self-consistent field. Dispersion interactions were incorporated with the van der Waals DF2 density functional method [71–73]. Dimensions of the simulation cell (32.84 Å, 34.63 Å and 32.12 Å) were adjusted to minimize effects on the energy of the system due to interactions across periodic boundaries. A time step of 0.5 fs and an energy cutoff of 400 eV were used. The temperature was held constant at 350 K with a Nose thermostat (period of 20 fs) to prevent the known over-structuring of water at 298 K when using PBE [74,75]. Hydrogen atoms were given the mass of deuterium to permit an increased simulation time step.

Chemical reactions were driven along a reaction coordinate defined by the distance between two selected atoms (distance labeled by red asterisk in Figs. S4–S7). The procedure decreases the atom–atom distance until the two atoms are bonded (~1.5 Å apart for C–O bonds and ~1.0 Å for O–H bonds). The driving is implemented in a stepwise manner by decreasing the atom–atom distance in 0.16-Å increments followed by 100 steps of simulation while constraining the reduced distance.

Electronic structure optimization and energy calculations

Electronic structure (QM) calculations, including optimizations to find lowest-energy structures and single-point energies of the simulated AIMD systems, were conducted with the Gaussian 09 program [76]. The four unstructured waters in the AIMD subsystem were omitted in these electronic structure calculations due to problems with the optimization of these mobile water molecules. QM subsystems for each of the reaction steps were optimized with the B3LYP [68–70] functional using the 6-31G(d) basis set as implemented in Gaussian 09. The B3LYP functional was chosen for the optimization process as it has been widely used and tested on organic chemistry systems, and it was the only functional that produced consistent optimized structures compared to others tested. The single-point energies of each optimized system were subsequently calculated with the more accurate M062X and ωB97X-D hybrid functionals and 6-311++G(2d,2p) basis set. The M062X functional has been shown to provide excellent performance for biologically relevant cases [77–79], and the more recent ωB97X-D functional [80] has been shown to describe accurately problems where charge transfer and dispersion are important [80–83]. Solvation effects were included in all calculations through the use of the integral equation formalism polarizable continuum model as implemented in Gaussian 09. A low dielectric constant, ε = 4, was chosen to resemble the internal protein environment. No significant difference in relative energies was observed when a value of ε = 40 was used instead.

Analysis of simulation results

All estimations of the contact probability and mobility of the atomic groups were performed for heavy (nonhydrogen) atoms only. Probabilities of contact between the enzyme, ligand and water molecules were scored based on the frequency of occurrence of the atoms within the first contact shell from each other. The width of the first shell was defined as the position of the first minimum on the time-averaged radial distribution function for all heavy atoms in ligand–enzyme and ligand–water contacts, which was close to 3 Å in all cases. Probability of contacts between the ligand and enzyme for unrestrained 30-ns simulations was calculated over the last 20 ns, with a time step of 10 ps. For the 1-ns simulations with restrained backbone, the contact probability was estimated with a 1-ps step and computed for the first 10 ps (to estimate the starting contacts, for comparison) and the last 100 ps.

Water molecules in direct contact with a ligand (first hydration shell, 3 Å distance between the centers of water oxygen and any heavy atom of the ligand) were estimated for each system with a 10-ps time step over the last 250 ps of the simulation period and averaged among all four catalytic sites.

The mobility of the ligand and enzyme residues was quantified as RMSF around time-averaged positions. It is known that straightforward interpretation of RMSF as residue mobility might be misleading if regions with a stable backbone conformation move as part of a larger secondary structural domain. In those cases, analysis of the backbone torsion angles is needed to provide a

complete picture of residue mobility [84]. However, such structural elements are not present in the catalytic site of L-ASP, which is lined by loops. Given that our mobility analysis is mainly focused on enzyme residues in close vicinity to the ligand, applied to the simulation stage with restrained backbone and intended to characterize the ligand and the enzyme motions, we have limited the quantification to RMSF. Alignment and calculations of the time-averaged position and fluctuations were performed for each catalytic site independently to avoid affecting the local ligand motions by remote changes in the domain positions or dynamics of other catalytic sites in the tetramer. The whole tetramer was split into four equal parts based on proximity to the nearest ligand. Spatial alignment for the catalytic site was performed based on all backbone atoms of the enzyme quarter. The final results of RMSF per atom for separate sites were averaged (as root of mean squares) among the catalytic sites to combine the statistics of the whole tetramer.

The distances between the particular atoms of interest were traced through time with a 1-ps step over the last 20 ns of simulations (see Fig. 6 and Fig. S8). The distances were traced independently for each catalytic site, and their frequencies were estimated and then averaged over all four catalytic sites. For presentation on the histograms, each distance was normalized relative to the sum of van der Waals radii (CHARMM27 values) of the two participating atoms.

RMSD measurements for Fig. 4 and Fig. S1 were performed by first spatially aligning the protein backbone with the starting configuration to account for translational and rotational motion. Contact RMSD values (Å) were calculated from protein residues in contact with the ligand: G11, T12, Y25, V27, G57, S58, Q59, G88, T89, D90, A114, M115, N248 and E283. Ligand RMSD values were calculated with respect to Asp in the crystal structure.

Acknowledgment

This work was supported by the Sandia Laboratory-Directed Research and Development Program and the Defense Threat Reduction Agency-Joint Science and Technology Office for Chemical and Biological Defense (IAA number DTRA100271A-03167). The work was also supported by a gift from the H. A. and Mary K. Chapman Foundations and a grant from the Michael and Susan Dell Foundation honoring Lorraine Dell. Sandia National Laboratories is a multiprogram laboratory operated by Sandia Corp., a wholly owned subsidiary of Lockheed Martin Corp., for the US Department of Energy's National Nuclear Security Administration under contract DE-AC04-94AL85000.

Appendix A. Supplementary data

Supplementary data to this article can be found online at <http://dx.doi.org/10.1016/j.jmb.2015.06.017>.

Received 21 January 2015;

Received in revised form 20 May 2015;

Accepted 26 June 2015

Available online 2 July 2015

Keywords:

enzyme kinetics;
molecular dynamics;
mass spectrometry (MS);
enzyme catalysis;
ab initio simulations

Present address: D. M. Rogers, Department of Chemistry,
University of South Florida, Tampa, FL 33620, USA.

†<http://propka.ki.ku.dk/>.

Abbreviations used:

LC-MS/MS, liquid chromatography–tandem mass spectrometry; MD, molecular dynamics; AIMD, *ab initio* MD; RMSF, root-mean-square fluctuation; QM, quantum mechanics; PBE, Perdew, Burke and Ernzerhof.

References

- [1] D. Covini, S. Tardito, O. Bussolati, L.R. Chiarelli, M.V. Pasquetto, R. Digilio, et al., Expanding targets for a metabolic therapy of cancer: L-Asparaginase, *Recent Pat. Anticancer Drug Discov.* 7 (2012) 4–13.
- [2] N.L. Kobrinsky, R. Sposto, N.R. Shah, J.R. Anderson, C. DeLaat, M. Morse, et al., Outcomes of treatment of children and adolescents with recurrent non-Hodgkin's lymphoma and Hodgkin's disease with dexamethasone, etoposide, cisplatin, cytarabine, and l-asparaginase, maintenance chemotherapy, and transplantation: Children's Cancer Group Study CCG-5912, *J. Clin. Oncol.* 19 (2001) 2390–2396.
- [3] M.E.J. Beard, D. Crowther, D.A.G. Galton, R.J. Guyer, G.H. Fairley, H.E.M. Kay, et al., L-Asparaginase in treatment of acute leukaemia and lymphosarcoma, *Br. Med. J.* 1 (1970) 191–195.
- [4] C. Derst, J. Henseling, K.H. Röhm, Engineering the substrate specificity of *Escherichia coli* asparaginase II. Selective reduction of glutaminase activity by amino acid replacements at position 248, *Protein Sci.* 9 (2000) 2009–2017.
- [5] D.N. Wheatley, Arginine deprivation and metabolomics: Important aspects of intermediary metabolism in relation to the differential sensitivity of normal and tumour cells, *Semin. Cancer Biol.* 15 (2005) 247–253.
- [6] A. Puissant, G. Robert, P. Auberger, Targeting autophagy to fight hematopoietic malignancies, *Cell Cycle* 9 (2010) 3470–3478.
- [7] R.P. Warrell, Z.A. Arlin, T.S. Gee, T.C. Chou, J. Roberts, C.W. Young, Clinical evaluation of succinylated *Acinetobacter* glutaminase-asparaginase in adult leukemia, *Cancer Treat. Rep.* 66 (1982) 1479–1485.
- [8] G. Ollenschläger, E. Roth, W. Linkesch, S. Jansen, A. Simmel, B. Mödder, Asparaginase-induced derangements of glutamine metabolism: The pathogenetic basis for some drug-related side-effects, *Eur. J. Clin. Investig.* 18 (1988) 512–516.
- [9] R.B. Reinert, L.M. Oberle, S.A. Wek, P. Bunpo, X.P. Wang, I. Mileva, et al., Role of glutamine depletion in directing tissue-

- specific nutrient stress responses to L-asparaginase, *J. Biol. Chem.* 281 (2006) 31222–31233.
- [10] P. Bunpo, B. Murray, J. Cundiff, E. Brizius, C.J. Aldrich, T.G. Anthony, Alanyl-glutamine consumption modifies the suppressive effect of L-asparaginase on lymphocyte populations in mice, *J. Nutr.* 138 (2008) 338–343.
- [11] H.J. Müller, J. Boos, Use of L-asparaginase in childhood ALL, *Crit. Rev. Oncol. Hematol.* 28 (1998) 97–113.
- [12] L.B. Silverman, R.D. Gelber, V.K. Dalton, B.L. Asselin, R.D. Barr, L.A. Clavell, et al., Improved outcome for children with acute lymphoblastic leukemia: Results of Dana-Farber Consortium Protocol 91-01, *Blood* 97 (2001) 1211–1218.
- [13] D. Kafkewitz, A. Bendich, Enzyme-induced asparagine and glutamine depletion and immune system function, *Am. J. Clin. Nutr.* 37 (1983) 1025–1030.
- [14] V.I. Avramis, E.H. Panosyan, Pharmacokinetic/pharmacodynamic relationships of asparaginase formulations: The past, the present and recommendations for the future, *Clin. Pharmacokinet.* 44 (2005) 367–393.
- [15] A.M. Aslanian, B.S. Fletcher, M.S. Kilberg, Asparagine synthetase expression alone is sufficient to induce L-asparaginase resistance in MOLT-4 human leukaemia cells, *Biochem. J.* 357 (2001) 321–328.
- [16] P.L. Lorenzi, J. Llamas, M. Gunsior, L. Ozbun, W.C. Reinhold, S. Varma, et al., Asparagine synthetase is a predictive biomarker of L-asparaginase activity in ovarian cancer cell lines, *Mol. Cancer Ther.* 7 (2008) 3123–3128.
- [17] W.K. Chan, P.L. Lorenzi, A. Anishkin, P. Purwaha, D.M. Rogers, S. Sukharev, et al., The glutaminase activity of L-asparaginase is not required for anticancer activity against ASNS-negative cell lines, *Blood* 123 (2014) 3596–3606.
- [18] J. Lubkowski, G.J. Palm, G.L. Gilliland, C. Derst, K.H. Röhm, A. Wlodawer, Crystal structure and amino acid sequence of *Wolinella succinogenes* L-asparaginase, *Eur. J. Biochem.* 241 (1996) 201–207.
- [19] J. Krasotkina, A.A. Borisova, Y.V. Gervaziev, N.N. Sokolov, One-step purification and kinetic properties of the recombinant L-asparaginase from *Erwinia carotovora*, *Biotechnol. Appl. Biochem.* 39 (2004) 215–221.
- [20] G.A. Kotzia, N.E. Labrou, Cloning, expression and characterisation of *Erwinia carotovora* L-asparaginase, *J. Biotechnol.* 119 (2005) 309–323.
- [21] D. Cappelletti, L.R. Chiarelli, M.V. Pasquetto, S. Stivala, G. Valentini, C. Scotti, *Helicobacter pylori* L-asparaginase: A promising chemotherapeutic agent, *Biochem. Biophys. Res. Commun.* 377 (2008) 1222–1226.
- [22] O.V. Kravchenko, Y.A. Kisiltsin, A.N. Popov, S.V. Nikonov, I.P. Kuranova, Three-dimensional structures of L-asparaginase from *Erwinia carotovora* complexed with aspartate and glutamate, *Acta Crystallogr. D Biol. Crystallogr.* 64 (2008) 248–256.
- [23] M. Ehrman, H. Cedar, J.H. Schwartz, L-Asparaginase II of *Escherichia coli*. Studies on the enzymatic mechanism of action, *J. Biol. Chem.* 246 (1971) 88–94.
- [24] J.B. Howard, F.H. Carpenter, L-Asparaginase from *Erwinia carotovora*. Substrate specificity and enzymatic properties, *J. Biol. Chem.* 247 (1972) 1020–1030.
- [25] K.H. Röhm, R.L. Van Etten, The ^{18}O isotope effect in ^{13}C nuclear magnetic resonance spectroscopy: Mechanistic studies on asparaginase from *Escherichia coli*, *Arch. Biochem. Biophys.* 244 (1986) 128–136.
- [26] C. Derst, J. Henseling, K.H. Röhm, Probing the role of threonine and serine residues of *E. coli* asparaginase II by site-specific mutagenesis, *Protein Eng.* 5 (1992) 785–789.
- [27] C. Derst, A. Wehner, V. Specht, K.H. Röhm, States and functions of tyrosine residues in *Escherichia coli* asparaginase II, *Eur. J. Biochem.* 224 (1994) 533–540.
- [28] E. Ortlund, M.W. Lacombe, K. Lewinski, L. Lebioda, Reactions of *Pseudomonas* 7A glutaminase-asparaginase with diazo analogues of glutamine and asparagine result in unexpected covalent inhibitions and suggests an unusual catalytic triad Thr-Tyr-Glu, *Biochemistry* 39 (2000) 1199–1204.
- [29] K. Aghaiypour, A. Wlodawer, J. Lubkowski, Do bacterial L-asparaginases utilize a catalytic triad Thr-Tyr-Glu? *Biochim. Biophys. Acta* 1550 (2001) 117–128.
- [30] K. Aghaiypour, A. Wlodawer, J. Lubkowski, Structural basis for the activity and substrate specificity of *Erwinia chrysanthemi* L-asparaginase, *Biochemistry* 40 (2001) 5655–5664.
- [31] E. Harms, A. Wehner, H.-P. Aung, K.H. Röhm, A catalytic role for threonine-12 of *E. coli* asparaginase II as established by site-directed mutagenesis, *FEBS* 285 (1991) 55–58.
- [32] G.J. Palm, J. Lubkowski, C. Derst, S. Schleper, K.H. Röhm, A. Wlodawer, A covalently bound catalytic intermediate in *Escherichia coli* asparaginase: Crystal structure of a Thr-89-Val mutant, *FEBS Lett.* 390 (1996) 211–216.
- [33] S. Schleper, Kinetische Untersuchungen und Modellstudien zur Funktion essentieller Reste im aktiven Zentrum der L-Asparaginase II aus *E. coli*, (Ph.D. Thesis) University of Marburg, Marburg, 1999.
- [34] A.L. Swain, M. Jaskólski, D. Housset, J.K. Mohana Rao, A. Wlodawer, Crystal structure of *Escherichia coli* L-asparaginase, an enzyme used in cancer therapy, *Proc. Natl. Acad. Sci. U. S. A.* 90 (1993) 1474–1478.
- [35] H.-P. Aung, M. Bocola, S. Schleper, K.H. Röhm, Dynamics of a mobile loop at the active site of *Escherichia coli* asparaginase, *Biochim. Biophys. Acta* 1481 (2000) 349–359.
- [36] M. Sanches, J.A.R.G. Barbosa, R.T. de Oliveira, J. Abrahão Neto, I. Polikarpov, Structural comparison of *Escherichia coli* L-asparaginase in two monoclinic space groups, *Acta Crystallogr. D Biol. Crystallogr.* 59 (2003) 416–422.
- [37] D.S. Gestó, N.M.F.S.A. Cerqueira, P.A. Fernandes, M.J. Ramos, Unraveling the enigmatic mechanism of L-asparaginase II with QM/QM calculations, *J. Am. Chem. Soc.* 135 (2013) 7146–7158.
- [38] M.-K. Yun, A. Nourse, S.W. White, C.O. Rock, R.J. Heath, Crystal structure and allosteric regulation of the cytoplasmic *Escherichia coli* L-asparaginase I, *J. Mol. Biol.* 369 (2007) 794–811.
- [39] A. Wehner, E. Harms, M.P. Jennings, I.R. Beacham, C. Derst, P. Bast, et al., Site-specific mutagenesis of *Escherichia coli* asparaginase II. None of the three histidine residues is required for catalysis, *Eur. J. Biochem.* 208 (1992) 475–480.
- [40] V.I. Avramis, S. Sencer, A.P. Periclou, H. Sather, B.C. Bostrom, L.J. Cohen, et al., A randomized comparison of native *Escherichia coli* asparaginase and polyethylene glycol conjugated asparaginase for treatment of children with newly diagnosed standard-risk acute lymphoblastic leukemia: A Children's Cancer Group study, *Blood* 99 (2002) 1986–1994.
- [41] R.S. Grigoryan, E.H. Panosyan, N.L. Seibel, P.S. Gaynon, I.A. Avramis, V.I. Avramis, Changes of amino acid serum levels in pediatric patients with higher-risk acute lymphoblastic leukemia (CCG-1961), *In Vivo* 18 (2004) 107–112.
- [42] I.H. Segel, *Enzyme Kinetics*, John Wiley & Sons, New York, 1993.
- [43] K. Rifai, A. Das, J. Rosenau, T. Ernst, U. Kretschmer, H. Haller, et al., Changes in plasma amino acids during extracorporeal liver support by fractionated plasma separation and adsorption, *Artif. Organs* 34 (2010) 166–170.

- [44] M. Ramanadham, V.S. Jakkal, R. Chidambaram, Carboxyl group hydrogen bonding in X-ray protein structures analysed using neutron studies on amino acids, *FEBS Lett.* 323 (1993) 203–206.
- [45] S.J. Fisher, M.P. Blakeley, M. Cianci, S. McSweeney, J.R. Helliwell, Protonation-state determination in proteins using high-resolution X-ray crystallography: Effects of resolution and completeness, *Acta Crystallogr. D Biol. Crystallogr.* 68 (2012) 800–809.
- [46] M.H.M. Olsson, C.R. Søndergaard, M. Rostkowski, J.H. Jensen, PROPKA3: Consistent treatment of internal and surface residues in empirical pK_a predictions, *J. Chem. Theory Comput.* 7 (2011) 525–537.
- [47] C.R. Søndergaard, M.H.M. Olsson, M. Rostkowski, J.H. Jensen, Improved treatment of ligands and coupling effects in empirical calculation and rationalization of pK_a values, *J. Chem. Theory Comput.* 7 (2011) 2284–2295.
- [48] S. Kumar, M. Das, C.M. Hadad, K. Musier-Forsyth, Substrate and enzyme functional groups contribute to translational quality control by bacterial prolyl-tRNA synthetase, *J. Phys. Chem. B* 116 (2012) 6991–6999.
- [49] G.A. Cisneros, M. Wang, P. Silinski, M.C. Fitzgerald, W. Yang, The protein backbone makes important contributions to 4-oxalocrotonate tautomerase enzyme catalysis: Understanding from theory and experiment, *Biochemistry* 43 (2004) 6885–6892.
- [50] M. Widersten, R. Björnstedt, B. Mannervik, Involvement of the carboxyl groups of glutathione in the catalytic mechanism of human glutathione transferase A1-1, *Biochemistry* 35 (1996) 7731–7742.
- [51] P. Purwaha, P.L. Lorenzi, L.P. Silva, D.H. Hawke, J.N. Weinstein, Targeted metabolomic analysis of amino acid response to L-asparaginase in adherent cells, *Metabolomics* 10 (2014) 909–919.
- [52] E. Jones, T. Oliphant, P. Peterson, SciPy: Open source scientific tools for Python, 2001.
- [53] W. Humphrey, A. Dalke, K. Schulten, VMD—Visual molecular dynamics, *J. Mol. Graph.* 14 (1996) 33–38.
- [54] E.F. Pettersen, T.D. Goddard, C.C. Huang, G.S. Couch, D.M. Greenblatt, E.C. Meng, et al., UCSF Chimera—A visualization system for exploratory research and analysis, *J. Comput. Chem.* 25 (2004) 1605–1612.
- [55] H. Li, A.D. Robertson, J.H. Jensen, Very fast empirical prediction and rationalization of protein pK_a values, *Proteins* 61 (2005) 704–721.
- [56] D.C. Bas, D.M. Rogers, J.H. Jensen, Very fast prediction and rationalization of pK_a values for protein–ligand complexes, *Proteins* 73 (2008) 765–783.
- [57] J.C. Phillips, R. Braun, W. Wang, J. Gumbart, E. Tajkhorshid, E. Villa, et al., Scalable molecular dynamics with NAMD, *J. Comput. Chem.* 26 (2005) 1781–1802.
- [58] A.D. Mackerell, D. Bashford, M. Bellott, R.L. Dunbrack, J.D. Evanseck, M.J. Field, et al., All-atom empirical potential for molecular modeling and dynamics studies of proteins, *J. Phys. Chem. B* 102 (1998) 3586–3616.
- [59] A.D. Mackerell, M. Feig, C.L. Brooks, Extending the treatment of backbone energetics in protein force fields: Limitations of gas-phase quantum mechanics in reproducing protein conformational distributions in molecular dynamics simulations, *J. Comput. Chem.* 25 (2004) 1400–1415.
- [60] G. Kresse, J. Hafner, *Ab initio* molecular dynamics for liquid metals, *Phys. Rev. B* 47 (1993) 558–561.
- [61] G. Kresse, J. Hafner, *Ab initio* molecular-dynamics simulation of the liquid-metal-amorphous-semiconductor transition in germanium, *Phys. Rev. B* 49 (1994) 14251–14269.
- [62] G. Kresse, J. Furthmüller, Efficient iterative schemes for *ab initio* total-energy calculations using a plane-wave basis set, *Phys. Rev. B* 54 (1996) 11169–11186.
- [63] J.P. Perdew, K. Burke, M. Ernzerhof, Generalized gradient approximation made simple, *Phys. Rev. Lett.* 77 (1996) 3865–3868.
- [64] J.P. Perdew, K. Burke, M. Ernzerhof, Erratum: Generalized gradient approximation made simple, *Phys. Rev. Lett.* 77 (1996) 1396.
- [65] G. Kresse, D. Joubert, From ultrasoft pseudopotentials to the projector augmented-wave method, *Phys. Rev. B* 59 (1999) 1758.
- [66] Y. Zhao, D.G. Truhlar, Density functionals for noncovalent interaction energies of biological importance, *J. Chem. Theory Comput.* 3 (2007) 289–300.
- [67] D. Asthagiri, L.R. Pratt, J.D. Kress, *Ab initio* molecular dynamics and quasichemical study of $H^+(aq)$, *Proc. Natl. Acad. Sci. U. S. A.* 102 (2005) 6704–6708.
- [68] A.D. Becke, Density-functional thermochemistry. III. The role of exact exchange, *J. Chem. Phys.* 98 (1993) 5648.
- [69] C. Lee, W. Yang, R. Parr, Development of the Colle-Salvetti correlation-energy formula into a functional of the electron density, *Phys. Rev. B* 37 (1988) 785–789.
- [70] P.J. Stephens, F.J. Devlin, C.F. Chabalowski, M.J. Frisch, *Ab initio* calculation of vibrational absorption and circular-dichroism spectra using density-functional force-fields, *J. Phys. Chem.* 98 (1994) 11623–11627.
- [71] J. Klimeš, D.R. Bowler, A. Michaelides, Chemical accuracy for the van der Waals density functional, *J. Phys. Condens. Matter* 22 (2009) 022201.
- [72] J. Klimeš, D.R. Bowler, A. Michaelides, Van der Waals density functionals applied to solids, *Phys. Rev. B* 83 (2011) 195131.
- [73] K. Lee, E.D. Murray, L. Kong, B.I. Lundqvist, D.C. Langreth, Higher-accuracy van der Waals density functional, *Phys. Rev. B* 82 (2010) 081101.
- [74] J. VandeVondele, F. Mohamed, M. Krack, J. Hutter, M. Sprik, M. Parrinello, The influence of temperature and density functional models in *ab initio* molecular dynamics simulation of liquid water, *J. Chem. Phys.* 122 (2005) 014515–014517.
- [75] S.B. Rempe, T.R. Mattsson, K. Leung, On “the complete basis set limit” and plane-wave methods in first-principles simulations of water, *Phys. Chem. Chem. Phys.* 10 (2008) 4685–4686.
- [76] M.J. Frisch, G.W. Trucks, H.B. Schlegel, G.E. Scuseria, M.A. Robb, J.R. Cheeseman, et al., Gaussian 09, Revision D.01, Gaussian, Inc., Wallingford CT, 2009.
- [77] Y. Zhao, D.G. Truhlar, The M06 suite of density functionals for main group thermochemistry, thermochemical kinetics, noncovalent interactions, excited states, and transition elements: Two new functionals and systematic testing of four M06-class functionals and 12 other functionals, *Theor. Chem. Accounts* 120 (2008) 215–241.
- [78] Y. Zhao, D.G. Truhlar, Density functionals with broad applicability in chemistry, *Acc. Chem. Res.* 41 (2008) 157–167.
- [79] E.G. Hohenstein, S.T. Chill, C.D. Sherrill, Assessment of the performance of the M05–2X and M06–2X exchange-correlation functionals for noncovalent interactions in biomolecules, *J. Chem. Theory Comput.* 4 (2008) 1996–2000.
- [80] J.-D. Chai, M. Head-Gordon, Long-range corrected hybrid density functionals with damped atom–atom dispersion corrections, *Phys. Chem. Chem. Phys.* 10 (2008) 6615–6620.

-
- [81] Y.-S. Lin, C.-W. Tsai, G.-D. Li, J.-D. Chai, Long-range corrected hybrid meta-generalized-gradient approximations with dispersion corrections, *J. Chem. Phys.* 136 (2012) 154109.
- [82] Y.-S. Lin, G.-D. Li, S.-P. Mao, J.-D. Chai, Long-range corrected hybrid density functionals with improved dispersion corrections, *J. Chem. Theory Comput.* 9 (2013) 263–272.
- [83] M. Soniat, D.M. Rogers, S.B. Rempe, Dispersion- and exchange-corrected density functional theory for sodium ion hydration, *J. Chem. Theory Comput.* (2015) <http://dx.doi.org/10.1021/acs.jctc.5b00357>.
- [84] R. Caliandro, G. Rossetti, P. Carloni, Local fluctuations and conformational transitions in proteins, *J. Chem. Theory Comput.* 8 (2012) 4775–4785.